A98-31561 ICAS-98-3,8,2

VORTICAL FLOWFIELD STRUCTURE AT FORWARD SWEPT WING CONFIGURATIONS

Dr.-Ing. Christian Breitsamter
o. Prof. Dr.-Ing. Boris Laschka

Lehrstuhl für Fluidmechanik, Technische Universität München
Boltzmannstr. 15, 85748 Garching, Germany

Abstract

Comprehensive flowfield investigations have been carried out on forward swept wing configurations with wing sweep of −40 deg. The present study focus on a generic wing–body model complemented by aft swept canards. For the canard–off and canard–on configurations instantaneous velocities were measured in several cross–flow planes using advanced hot–wire anemometry. The tests were made at 10, 20, and 30 deg angle–of–attack at a Reynolds number of 0.46×10^6. Detailed surveys of mean and rms velocities show that free vortex sheets are generated at the wing leading–edge which roll up into strong leading–edge vortices. Their rotation is opposite to that of the tip vortices. Bursting over the wing occurs already at moderate angles of attack. At higher incidences a trailing–edge vortex is shed along the inner part of the wing which is counter–rotating in sense to the leading–edge vortex. The canard vortices pass the wing leading–edge relatively high, and after the onset of wing vortices they are moved upwards and outboard. The interference between these vortices is studied in detail analyzing the associated turbulent flow structure. Downstream of wing vortex bursting the highest turbulence intensities are found in an annular region around the vortex center, where fluctuations are channeled into a narrow–band.

Nomenclature

f	frequency, [Hz]
k	reduced frequency, $f\, l_\mu / U_\infty$
l_W	wing apex–tip distance, [m]
l_μ	wing mean aerodynamic chord, [m]
Re_{l_μ}	Reynolds number, $U_\infty l_\mu / \nu$
s	wing span, [m]
s_C	canard span, [m]
U_∞	freestream velocity, [m/s]
u, v, w	streamwise, lateral, and vertical velocity, [m/s]
$\overline{u}, \overline{v}, \overline{w}$	streamwise, lateral, and vertical mean velocity, [m/s]
u', v', w'	fluctuation part of u, v, w, [m/s]
u_{rms}, v_{rms}, w_{rms}	rms value of the fluctuating components of velocity, $u_{rms} = \sqrt{\overline{u'^2}}$, $v_{rms} = \sqrt{\overline{v'^2}}$, $w_{rms} = \sqrt{\overline{w'^2}}$
$\vec{\overline{u}}_{yz}$	mean cross–flow velocity vector
Y, Z	local nondimensionalized coordinates of the measurement plane, referred to s, origin at the midsection
$\tilde{x}_W, \tilde{y}_W, \tilde{z}_W$	wing–fuselage coordinates, origin at the nose, [m]
x, y, z	streamwise, lateral, and vertical coordinates of the wind–tunnel axis system, [m]
x_W, y_W, z_W	wing coordinates, origin at the tip, [m]
α	aircraft angle of attack, deg
ν	kinematic viscosity, [m^2/s]

Introduction

High agility and poststall maneuvering are key factors in the design of future generation fighter aircraft.[1,2] Consequently, there is a need for high turn rates within a wide operational range as well as the capability to perform tactical maneuvers beyond maximum lift. In this context, forward swept wing (FSW) configurations offer potential advantages.[3–6] FSWs are especially suited for close–coupled canards, as the canard leading–edge vortices have a favourable influence on the flow of the inner wing area resulting in high usable lift.[7,8]

Concerning aerodynamic, structural and aeroelastic properties the main benefits of FSW can be summarized as follows: For an equal wing box sweep the FSW leading–edge sweep is smaller than that of the aft swept wing (ASW) whereas the FSW trailing–edge sweep is greater. Hence, the maximum leading–edge suction produced by the FSW is achieved at higher incidences. Induced drag will be correspondingly lower through which maximum lift over drag ratios are improved, Fig. 1.

On ASWs maximum lift is limited by tip stall at a lift coefficient for which the large inner wing area is far from its limiting lift. For negative wing sweep the aerodynamic lifting potential of the inner wing is exploited to an ever increasing degree. Because of this, the FSW can be expected to produce a higher maximum lift coefficient than the ASW. An untwisted FSW

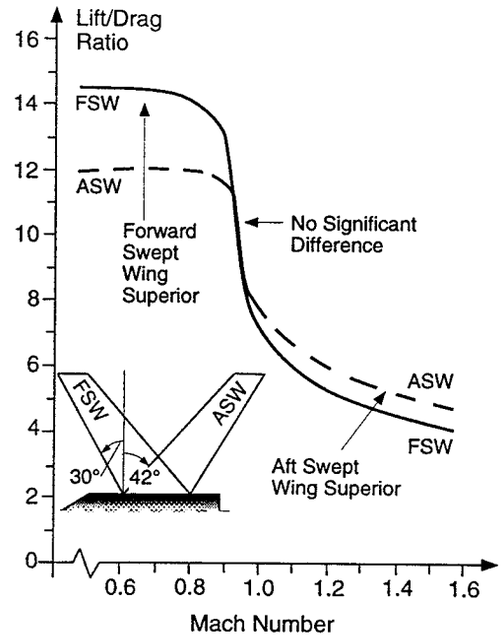

FIGURE 1 – Comparison of the maximum lift/drag ratios of FSW and ASW (of the same area and aspect ratio), Ref. 8

with an aeroisoclinic behaviour may exhibit an almost ideal lift distribution at all subsonic points of the flight envelope.[9] At high subsonic Mach numbers the FSW will sustain a higher pre–shock Mach number and hence a larger lift coefficient for the same pressure jump across the shock. For the high–speed flight regime there are no significant profits.

In general, on ASWs boundary layer separation begins in the tip region whereas on FSWs the root area stalls first. Due to the smaller roll and yaw disturbances and the undiminished roll control power, flow separation effects such as wing drop, wing rock and nose slice may be considerably less severe on FSWs. Therefore, FSW configurations are stable in yaw and roll up to high angles of attack. Moreover, the relocation of wing lift from the tip region to the root area provides the FSW with high aileron effectiveness even beyond maximum lift. Thus, there are appreciable advantages at subsonic speeds, in particular, for the high angle of attack performance. For weight reduction the lower tip aerodynamic loading of FSWs allows the use of a higher wing taper on the FSW than is possible for the ASW.[10]

The main aeroelastic disadvantage of the FSW is the reduction in divergence speed as sweep is reduced from aft to forward. It has been the main reason for not exploiting the aerodynamic benefits of FSWs in high–performance fighter aircraft. The introduction of carbon–fibre composites in aircraft structures has eliminated this obstacle. The FSW main aeroelastic advantage is its aileron efficiency and the very high aileron reversal speed. For the same reason, active control technology, using outboard flaps, could be applied more efficiently on FSWs.

Extensive investigations on the FSW aerodynamic characteristics were performed in the decade from 1975 to 1985 to develop the FSW concept for flight demonstration.[6,8,10–12] The efforts result in the X–29A FSW advanced technology demonstrator program[13] integrating key technologies like close coupled canards, supercritical airfoil, variabel camber, aeroelastic tailoring, and composite primary structure. However, for FSW configurations only few flowfield studies were reported. Griffin,[14] and Griffin et al.[15,16] presented distributions of steady cross–flow velocities and total pressure coefficients. Unsteady flowfields were not measured. As a contribution to fill this gap, a research program on generic FSW configurations was initiated at the Lehrstuhl für Fluidmechanik of the Technische Universität München.[17]

Present Scope and Objectives

The investigations are aimed at providing detailed insight into the flow physics of FSW configurations. Systematic aerodynamic tests have been conducted which focus on the flow phenomena at moderate and high angles of attack. In particular, the complex vortex systems are studied comparing the separation topology with the known features of delta and of aft swept wings. The results obtained contribute to the knowledge on leading–edge vortex flows which is essential for future fighter aircraft design. The turbulent flow structure is also carefully investigated. The related data base is needed to quantify the excitation input associated with aeroelastic phenomena like buffeting on wing or fin(s). Moreover, the comprehensive flowfield surveys are of distinct utility for the development and validation of CFD methods.

Measurement Technique and Test Program

Description of Models and Facility

The experiments were performed on a single 40 deg forward swept wing as well as on a generic wing–body configuration fitted with the identical wing planform, Fig. 2. The modular conception of the wing–body model enables the mounting of canards and/or strakes. The canards can be fixed in two vertical and eight axial positions featuring aft or forward leading–edge sweep. The geometric data of the configurations tested are collected in Table 1. This paper presents results of the investigations on the wing–body model with and without an aft swept canard. The airfoil of the wing and canard is the NACA 64A10. The fuselage of the wing–body model is formed as an elliptic cylinder with a canopy. The nose section is inclined downwards at an

angle of 5 deg. All model parts are made of carbon–fibre composites with steel inlets.

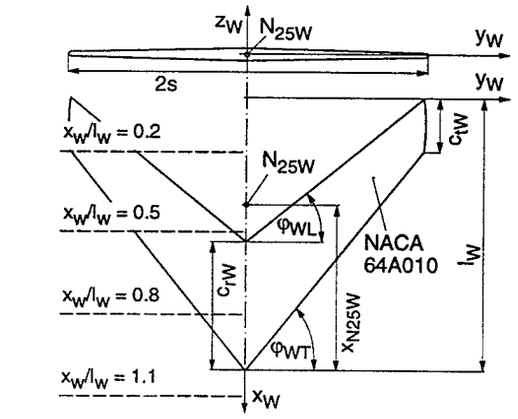

a) Wing geometry

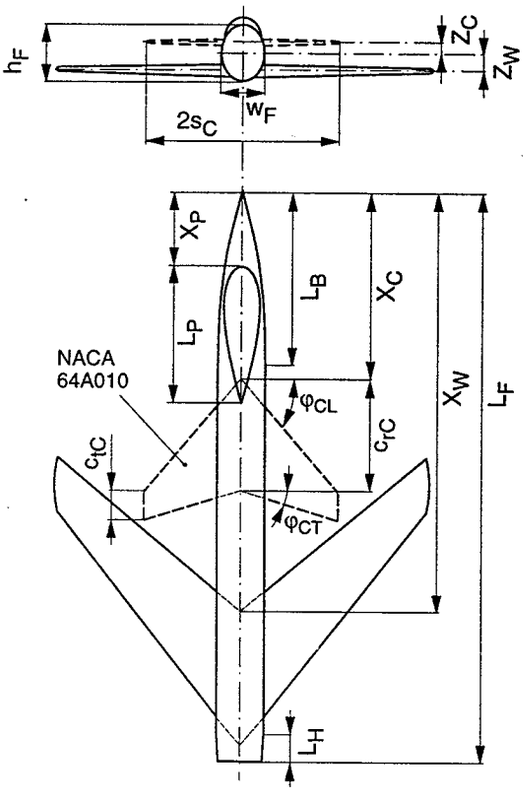

b) Wing–fuselage/wing–fuselage–canard geometry

FIGURE 2 – Wing, wing–fuselage, and wing–fuselage–canard configuration

The experiments were carried out in the 1.5 m low–speed wind tunnel facility of the Lehrstuhl für Fluidmechanik of the Technische Universität München. The wind tunnel is of the Göttingen–type with an open test section of circular shape. The wind tunnel geometric and operational data are given in Table 2.

The test section is equipped with a three–axis model support and a three–degree–of–freedom probe–traversing system. The models were sting mounted on their lower surfaces from the moving support strut, Fig. 3. This arrangement ensures that flowfield measurements are to a great extent free from interference. The computer controlled model support strut provides an incidence range from 0 to 31.5 deg and the models may be yawed and rolled 360 deg. Probes can be traversed in the streamwise, spanwise and normal directions with minimum steps of ±0.2 mm.

Wing	
Leading–edge sweep	$\varphi_{WL} = -40.0°$
Trailing–edge sweep	$\varphi_{WT} = -52.2°$
Aspect ratio	$A_W = 3.81$
Taper ratio	$c_{tW}/c_{rW} = 0.40$
Span	$2\,s = 0.60\ m$
Mean aerodynamic chord	$l_\mu = 0.167\ m$
Geo. neutr. point N_{25_W}	$x_{N25_W}/l_W = 0.354$
Canard	
Leading–edge sweep	$\varphi_{CL} = 49.0°$
Trailing–edge sweep	$\varphi_{CT} = 25.5°$
Aspect ratio	$A_C = 3.14$
Taper ratio	$c_{tC}/c_{rC} = 0.30$
Relative span	$s_C/s = 0.54$
Fuselage	
Length/height ratio	$L_F/h_F = 10$
Height/width ratio	$h_F/w_F = 1.19$
Front part length	$L_B/h_F = 2.63$
Rear part length	$L_H/h_F = 0.53$
Canopy length	$L_P/h_F = 2.37$
Position of canopy	$X_p/L_F = 0.13$
Combination Wing–Fuselage	
Relative fuselage length	$L_F/2\,s = 1.58$
Relative fuselage width	$w_F/2\,s = 0.13$
Relative wing position	$X_W/L_F = 0.74$
	$Z_W/h_F = 0.32$
Combination Canard–Fuselage	
Relative canard position	$X_C/L_F = 0.32$
	$Z_C/h_F = 0.21$

TABLE 1 – Geometric parameters of wind–tunnel models

Nozzle diameter	1.50 m
Length of test section	3.00 m
Maximum power	85 kW
Maximum usable velocity	55 m/s
Turbulence intensity	0.3% – 0.4%

TABLE 2 – Operational data of wind tunnel facility

Measurement of Instantaneous Velocity

In order to measure the fluctuating velocities dual–sensor hot–wire probes (DISA 55P61) were used. The sensors consist of 5–μm–diam. platinum–plated tungsten wires giving a length/diam. ratio of 250. The mea-

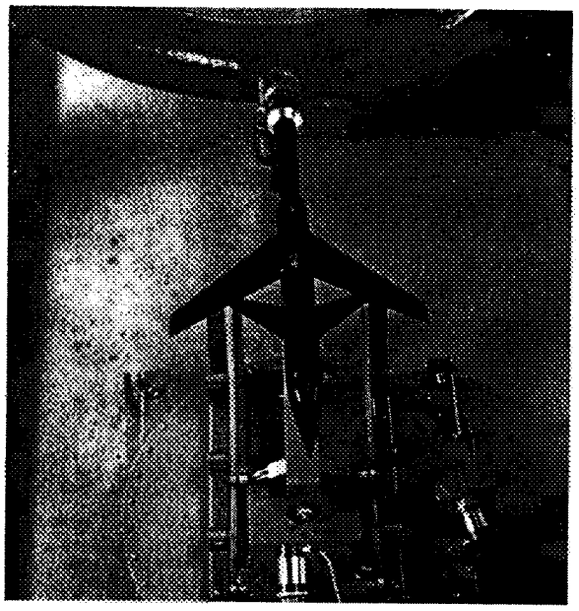

FIGURE 3 – Wing–body–canard model mounted in the test section

suring volume formed by the wires was approximately 0.8 mm in diam. and 0.5 mm in height. A sensor angle of 45 deg was chosen assuming that the best angular resolution will be obtained with pairs of perpendicular wires. An additional temperature probe was employed to correct the anemometer output–voltages if ambient flow temperature varies.

The probes were operated by a multi–channel constant–temperature anemometer system (DANTEC). By means of its signal conditioner modules, bridge output voltages were low–pass filtered at 1000 Hz before digitization and amplified for optimal signal level. The signals were then digitized with 12–bit precision through the sixteen–channel simultaneous–sampling A/D converter of the PC high–speed board. The sampling rate for each channel was set to 3000 Hz giving a Nyquist frequency of 1500 Hz. The sampling time was 26.24 sec so that each sample block contains 78720 points. These parameters were achieved by preliminary tests to ensure that all significant flowfield phenomena were detected. Statistical accuracy of the calculated quantities was considered as well. Random error calculations gave accuracies of 0.2, 1, and 3% for the mean and standard deviation and spectral density estimation, respectively.[18]

The use of a cross–wire configuration generally assumes some knowledge of the flowfield, such as a known flow direction to which the probe must be aligned. The nature of the vortex–dominated flow precludes any knowledge on the direction of the velocity vector everywhere in the field, save for the axial component which is assumed to be always in the positive x–direction. In order to determine the three velocity components (u, v, w) the probe has to be rotated around its axis by 90 deg to adjust the wire plane once horizontal and once vertical against the main flow direction (quadrupel–probe). Thus, two triggered traverse sweeps were necessary to obtain the streamwise (u), lateral (v) and vertical (w) components, respectively. Each digitized and temperature corrected voltage–pair of the corresponding probe positions was converted to evaluate the time–dependent velocity vector. The numerical method used is based on look-up tables derived from the full velocity– and flow angle calibration of the sensors. A detailed description is given in Refs. 19 and 20.

Description of Tests

Flowfield measurements were conducted in four planes perpendicular to the model x_W–axis. Three planes were located over the port wing at stations $x_W/l_W = 0.2$, 0.5, and 0.8, and one in the wake at $x_W/l_W = 1.1$ (Fig. 2). The tests were carried out at angles of attack of 10, 20, and 30 deg at symmetric freestream with constant reference velocity U_∞ of 40 m/s. This corresponds to a Reynolds number of $Re_{l_\mu} = 0.46 \times 10^6$ based on the wing mean aerodynamic chord for all the results presented. Local atmospheric conditions prescribed the test section static pressure and temperature. Within these experiments transition was not fixed.

For all measurement planes the lateral distance was fixed at 1.1 s, thus covering all relevant flowfield phenomena. The vertical extension was adapted to the expansion of the vortex systems known from laser light sheet tests. The survey points were evenly spaced, giving a relative grid resolution of 0.016 in both the spanwise and vertical direction based on the wing span. This is illustrated by Fig. 4 depicting size and grid of the measurement planes for the wing–fuselage tests at $\alpha = 20$ deg.

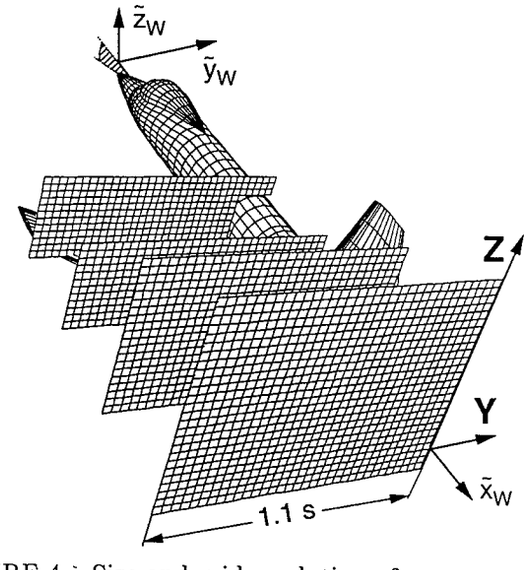

FIGURE 4 – Size and grid resolution of measurement planes used for wing–fuselage tests at $\alpha = 20$ deg

Results and Discussion

Flow Visualization

Laser light sheet tests were made to determine the evolution of the vortex systems, mainly produced by the forward swept wing (FSW) and, for the canard–on configuration by the aft swept canard. Results shown here depict light sheets at $x_W/l_W = 0.5$, and 1.1 obtained for canard–off at $\alpha = 30$ deg, Fig. 5. At $x_W/l_W = 0.5$ the cross section of the FSW leading–edge vortex is of elliptical shape and has strongly expanded indicating that bursting occurs far upstream. The tip vortex is well defined by the corresponding rolled up shear layers. Downstream at $x_W/l_W = 1.1$, the FSW leading–edge vortex becomes further enlarged resulting in a big region of highly fluctuating flow. The tip vortex grows also in size. An additional vortical structure can be identified behind the inner wing part representing the wing trailing–edge vortex. Based on the laser light sheet tests, survey locations and extensions of the time consuming probe measurements were defined.

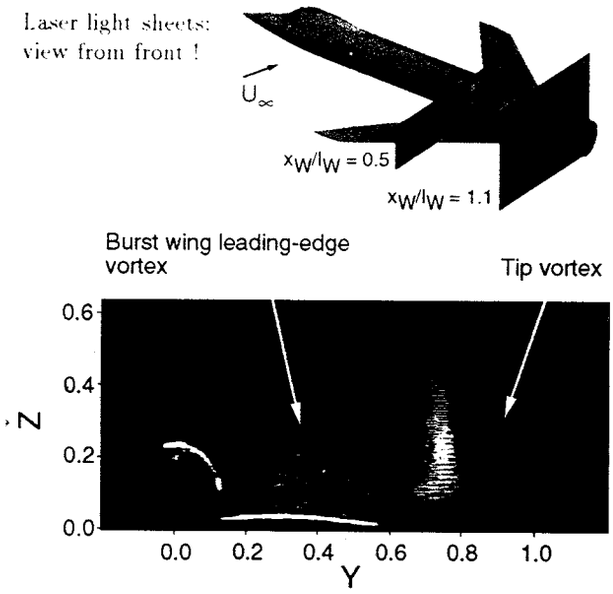

a) Measurement station $x_W/l_W = 0.5$

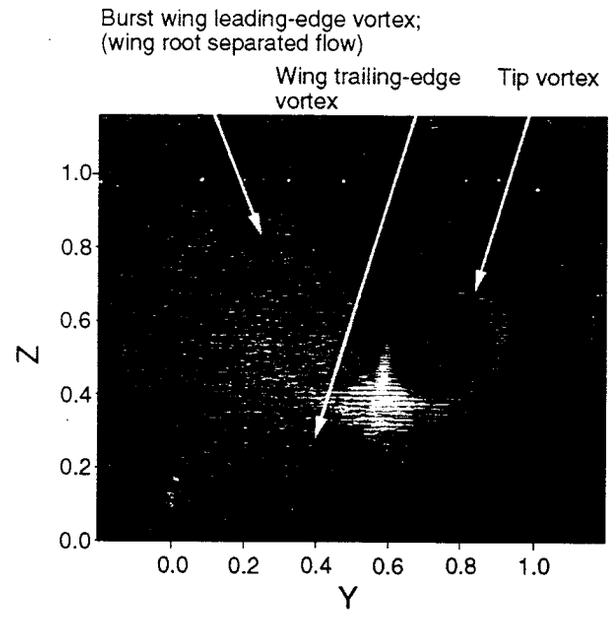

b) Measurement station $x_W/l_W = 1.1$

FIGURE 5 – Laser light sheet flow visualization for the wing–body configuration at $\alpha = 30$ deg

Mean Velocity Surveys

The three–dimensional flowfield over the port wing is documented both by cross–flow velocity vectors, Figs. 6 and 7, and by contours of streamwise and lateral velocities, Figs. 8 to 11. The flowfields of the wing–body and wing–body–canard configuration are characterized by the interaction of several vortex systems. At $\alpha = 20$ deg, the FSW tip and leading–edge vortex as well as the canard leading– and trailing–edge vortex are clearly visible by the induced cross–flow velocities, Figs. 6a, 7a. Contrary to delta or aft swept wings, the tip and leading–edge (primary) vortex of the FSW are counter–rotating. For both the canard–on and canard–off configuration even in the most upstream plane the cross section of the wing leading–edge vortex is elliptically formed and a region of reduced velocity dominates the vortex core. This indicates that the wing leading–edge vortex is already bursted. From oilflow patterns the burst position is determined at $x_W/l_W = 0.11$ for the wing–body and at $x_W/l_W = 0.16$ for the wing–body–canard configuration, respectively.[21] With increasing incidence, $\alpha = 30$ deg, the vortex systems are strongly enlarged producing higher cross flow components than at $\alpha = 20$ deg, Figs. 6b, 7b. Bursting of the wing leading–edge vortex takes place close to the wing tip, particularly, at $x_W/l_W = 0.05$ for the wing–body and at $x_W/l_W = 0.09$ for the wing–body–canard configuration.[21] Thus, the wing leading–edge vortex shows a big core region of very low velocity. The canard leading–edge vortex is bursted at $\alpha = 20$, and 30 deg as well. However, over the wing a more concentrated canard vortex system can be observed.

At $\alpha = 20$ deg and $x_W/l_W = 0.2$, the wing–body mean velocity distribution indicates the center of the wing tip vortex by the peak axial velocity ($\overline{u}/U_\infty = 1.75$) at $Y = -1.01, Z = -0.20$, Fig. 8a. For the burst wing leading–edge vortex the center is detected by a minimum of axial velocity ($\overline{u}/U_\infty = 0.85$) at $Y = -0.72, Z = -0.22$. A secondary vortex is located at $Y = -0.64, Z = -0.24$, Figs. 8a, 10a. The secondary vortex is rather small since the boundary layer on the wing beneath the leading–edge vortex is turbulent. At $x_W/l_W = 0.5$ the core of the burst wing leading–edge vortex increases strongly in its radial extension. It shows an axial velocity deficit with $\overline{u}/U_\infty = 0.45$, Fig. 8b. Above and below the core region the axial flow

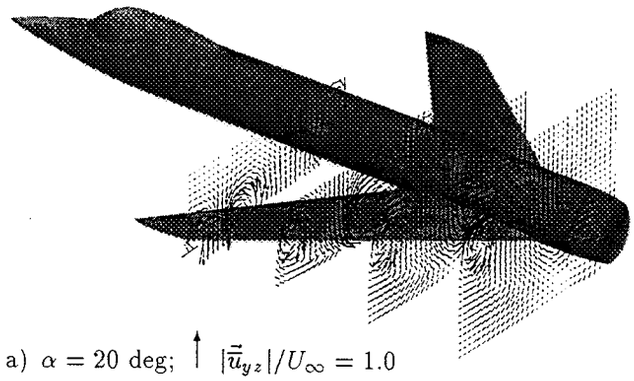

a) $\alpha = 20$ deg; $\uparrow |\vec{\overline{u}}_{yz}|/U_\infty = 1.0$

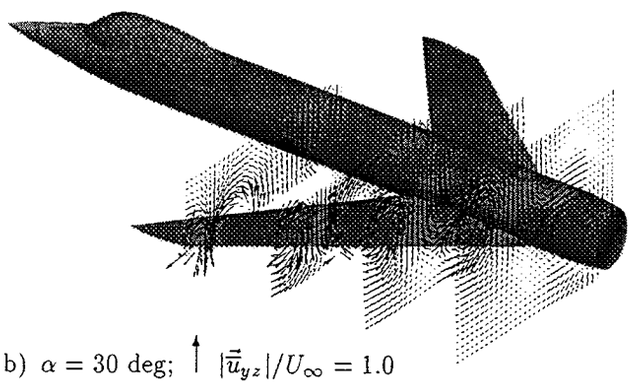

b) $\alpha = 30$ deg; $\uparrow |\vec{\overline{u}}_{yz}|/U_\infty = 1.0$

FIGURE 6 – Wing-body cross flow velocity vectors $\vec{\overline{u}}_{yz}$ at measurement planes $x_W/l_W = 0.2, 0.5, 0.8, 1.1$ for $\alpha = 20$, and 30 deg

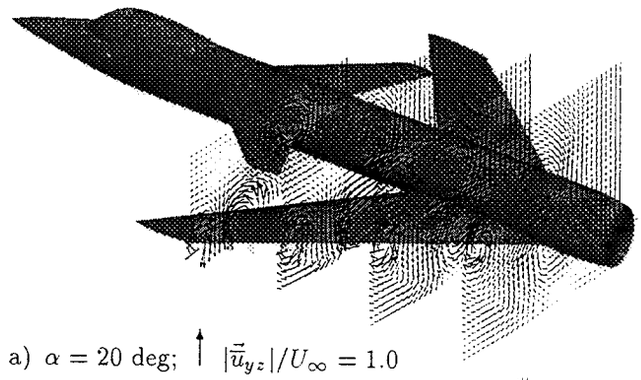

a) $\alpha = 20$ deg; $\uparrow |\vec{\overline{u}}_{yz}|/U_\infty = 1.0$

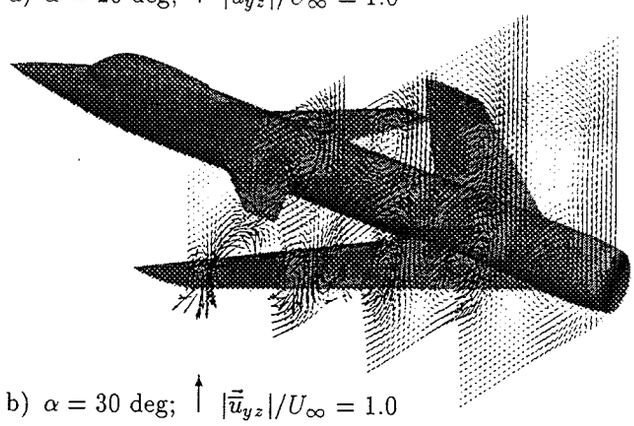

b) $\alpha = 30$ deg; $\uparrow |\vec{\overline{u}}_{yz}|/U_\infty = 1.0$

FIGURE 7 – Wing-body-canard cross flow velocity vectors $\vec{\overline{u}}_{yz}$ at measurement planes $x_W/l_W = 0.2, 0.5, 0.8, 1.1$ for $\alpha = 20$, and 30 deg

is accelerated reaching a maximum of $\overline{u}/U_\infty = 1.65$ close to the wing surface. The induced lateral velocity is 30% of U_∞ above the core and 50% of U_∞ near the wing surface, Fig. 10b. There, the deflection of the flow is inwards whereas on an ASW this deflection is outwards. Downstream at $x_W/l_W = 0.8$, the leading–edge vortex moves further inboard and upwards, Fig. 8c. Thus, above the fuselage the port wing vortex sheets come in contact with the starboard ones. Although the vortex core becomes very large, a well–structured swirling flow pattern can be observed around it. At $Y = -0.38, Z = -0.21$, a trailing–edge vortex is found with a rotation opposite to the one of the leading–edge vortex, Fig. 10c. More downstream the trailing–edge vortex is embedded in the shear layer of the dominant leading–edge vortex. In the wake ($x_W/l_W = 1.1$) the wing primary vortex starts to dissipate but it is strong enough to move the trailing–edge vortex inboard and upwards.[17]

For the wing–body–canard configuration the overall vortex structure is significantly changed, Figs. 9, 11. At $x_W/l_W = 0.2$, the axial velocity contours denote that the canard vortex system consists of a burst leading–edge vortex ($Y = -0.35, Z = 0.06$) and a tip vortex combined with a trailing–edge vortex ($Y = -0.55, Z = 0.01$), Figs. 9a, 11a. Because of the canard influence the wing leading–edge vortex produces higher axial and lateral velocities compared to the canard–off configuration. Moreover, the inner portion of the wing encounters the accelerated flow evoked by the canard through which the wing leading–edge vortex is embedded in a higher suction level than for the noninterfering case. Therefore, in comparison to canard–off the burst position of the wing leading–edge vortex is shifted downstream. At $x_W/l_W = 0.5$ the canard vortex system pushes the wing leading–edge vortex downwards to the wing surface, Figs. 9b, 11b. The wing vortex strength is again higher than for canard–off. At $x_W/l_W = 0.8$, compared to the wing–body case the wing leading–edge vortex is also moved closer to the wing surface whereas the induced cross flow velocities are not markedly increased, Figs. 9c, 11c.

The presentation of these results reveal that there is a strong influence of the canard on the wing. The canard produces behind its trailing edge a downwash field within its span and an upwash field outside its span. The upwash field increases the effective angle of attack in the forward and outside portion of the wing which supports flow separation there. The downwash field reduces the effective angle of attack in the innner and rear portion of the wing. This leads to a suppression of flow separation there which is especially favourable for delaying stall at the wing root area. Due to the non-

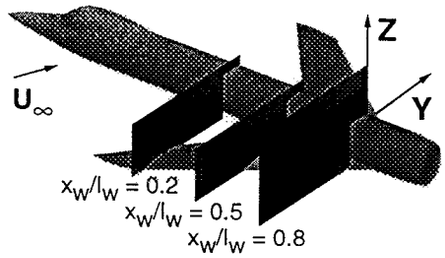

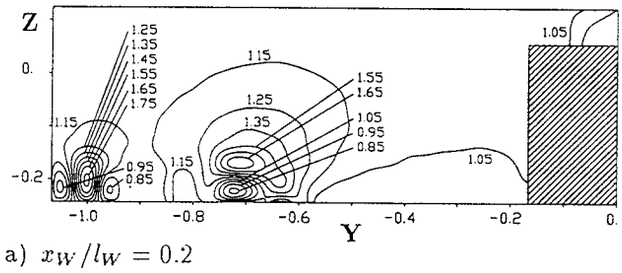

a) $x_W/l_W = 0.2$

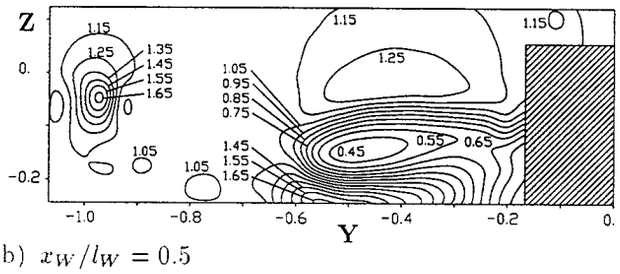

b) $x_W/l_W = 0.5$

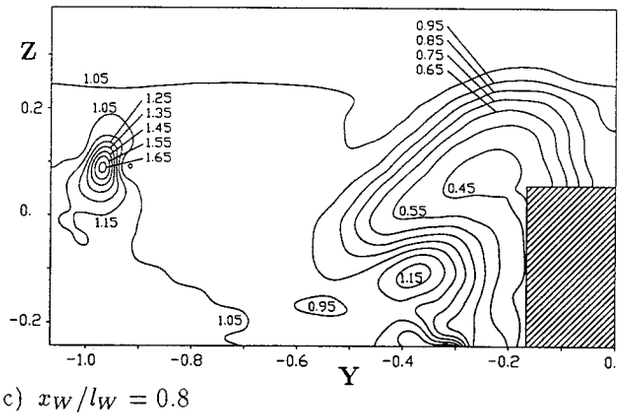

c) $x_W/l_W = 0.8$

FIGURE 8 – Contours of mean axial velocity $\overline{u}/U_\infty$ for the wing–body configuration at measurement planes $x_W/l_W = 0.2, 0.5, 0.8$, and $\alpha = 20$ deg

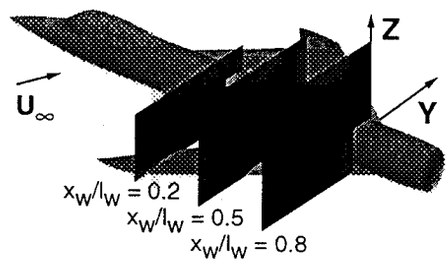

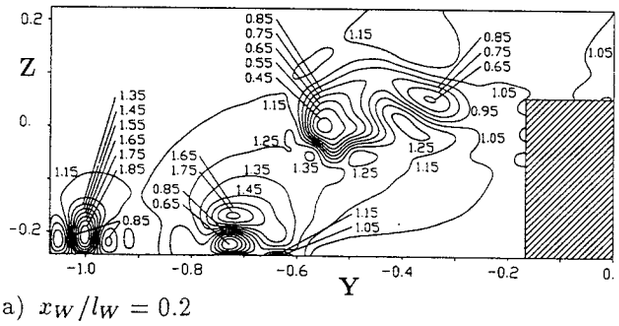

a) $x_W/l_W = 0.2$

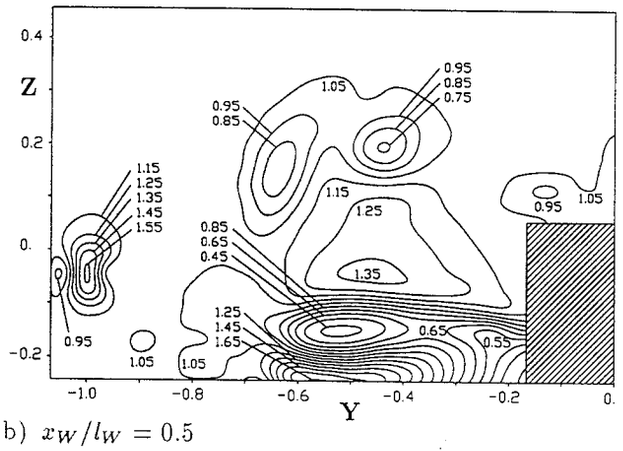

b) $x_W/l_W = 0.5$

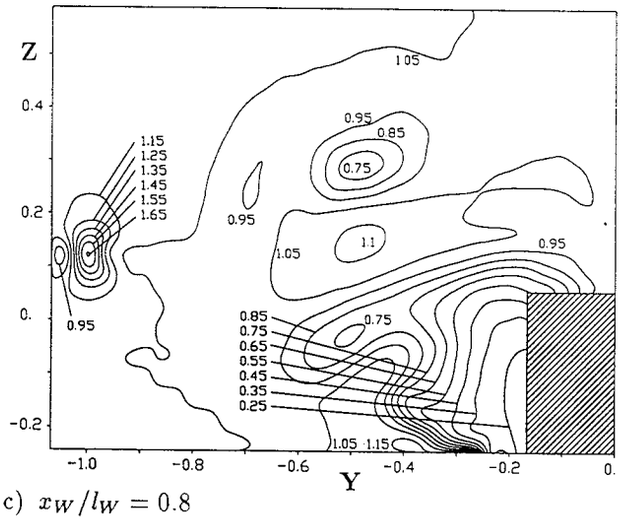

c) $x_W/l_W = 0.8$

FIGURE 9 – Contours of mean axial velocity $\overline{u}/U_\infty$ for the wing–body–canard configuration at measurement planes $x_W/l_W = 0.2, 0.5, 0.8$, and $\alpha = 20$ deg

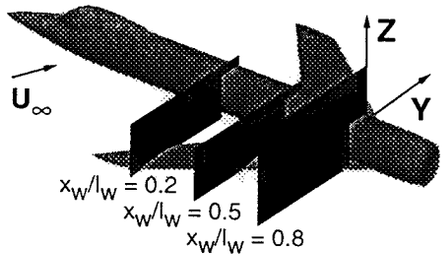

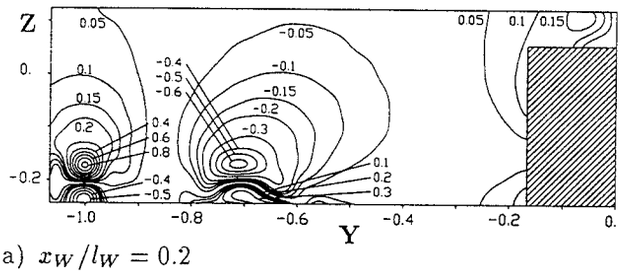

a) $x_W/l_W = 0.2$

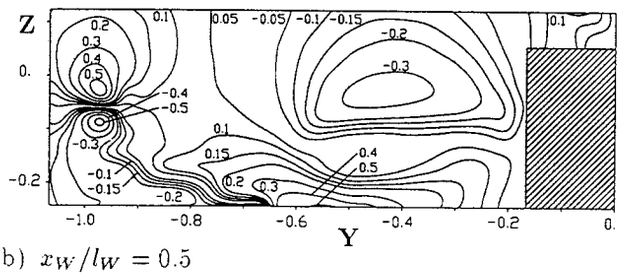

b) $x_W/l_W = 0.5$

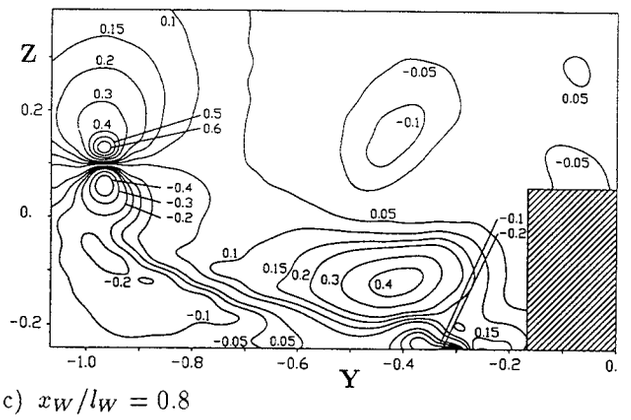

c) $x_W/l_W = 0.8$

FIGURE 10 – Contours of mean lateral velocity $\overline{v}/U_\infty$ for the wing–body configuration at measurement planes $x_W/l_W = 0.2, 0.5, 0.8$, and $\alpha = 20$ deg

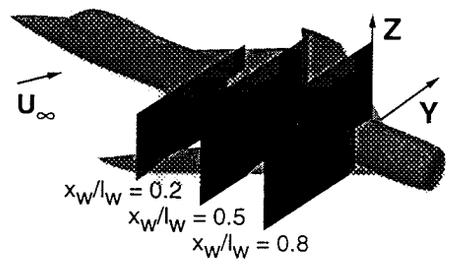

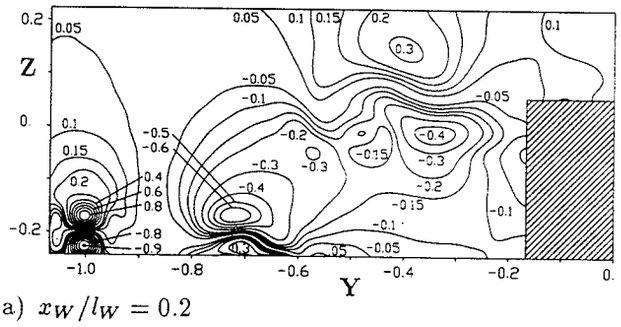

a) $x_W/l_W = 0.2$

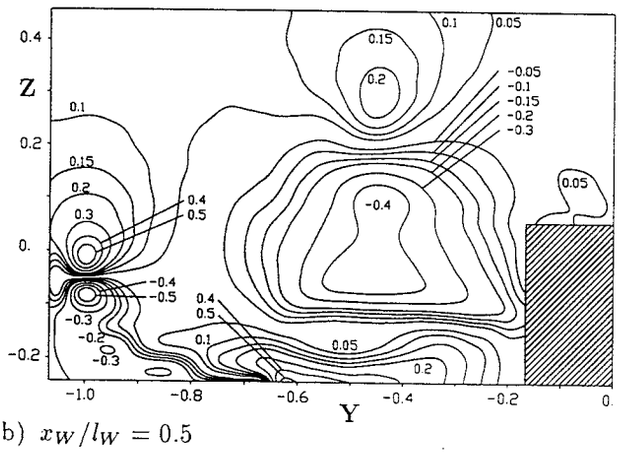

b) $x_W/l_W = 0.5$

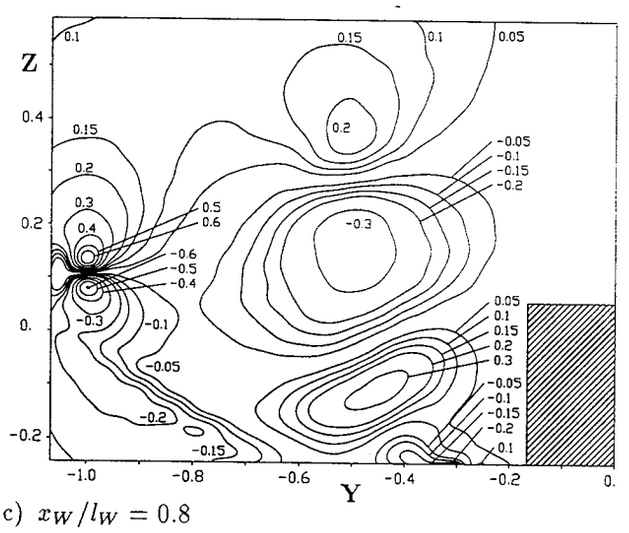

c) $x_W/l_W = 0.8$

FIGURE 11 – Contours of mean lateral velocity $\overline{v}/U_\infty$ for the wing–body–canard configuration at measurement planes $x_W/l_W = 0.2, 0.5, 0.8$, and $\alpha = 20$ deg

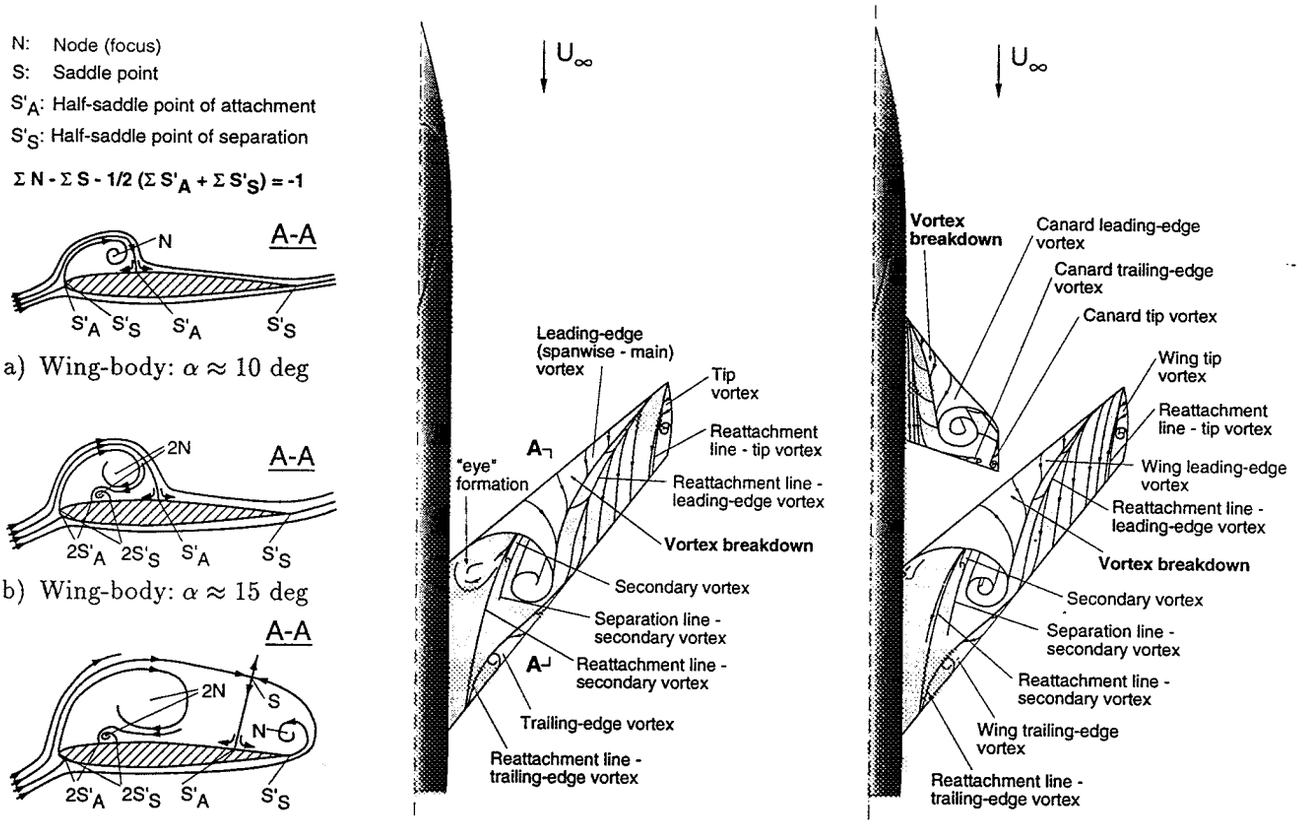

a) Wing-body: $\alpha \approx 10$ deg

b) Wing-body: $\alpha \approx 15$ deg

c) Wing-body: $\alpha \approx 20 - 30$ deg

d) Wing-body: $\alpha \approx 20 - 30$ deg

e) Wing–canard: $\alpha \approx 20 - 30$ deg

FIGURE 12 – Schematic representation of the vortex flow features at the wing–body and wing–body–canard configuration for moderate and high angles of attack

uniform distribution of the effective angle of attack along the wing leading–edge, the wing primary vortex is fed with vorticity in a different manner than for the canard–off configuration. For this reason the wing vortices evoke higher cross flow velocities in the outer wing part than for the noninterfering case. The influence of the wing leading–edge vortex on the canard vortices is such that the canard vortex system is moved outboard and upwards. The wing induced flow acceleration reinforces the canard vortex system over the wing, through which it still keeps its structure downstream behind the wing trailing–edge.

The development of the mean flowfield is summarized in Fig. 12 depicting the flow topology of an inner wing section from moderate to high angles of attack supplemented by a schematic three–dimensional representation. The topology rule used can be taken from Ref. 22. For moderate angles of attack a leading–edge vortex develops which is placed close to the wing surface, Fig. 12a. Bursting occurs already in the outer wing part. The vortex–induced pressure gradients are too small to cause a secondary separation. At higher incidences the leading–edge vortex grows both in size and strength that a secondary vortex is formed, Fig. 12b. With further increasing incidence the trailing–edge vortex sheet emanating from the inner wing rolls up into a trailing–edge vortex, the rotation of which is opposite to the leading–edge vortex, Fig. 12c. The axis of the leading–edge vortex initially points inboard on the wing, before being aligned with the freestream direction. At canard–off the wing root area is then characterized by a disorganized, separated flow, Fig. 12d. At high α the canard vortex system consist also of a leading–edge vortex, a small trailing–edge vortex and a tip (side–edge) vortex, Fig. 12e. At canard–on the strength of the wing leading–edge vortex is increased in the outside portion of the wing. Moreover, the wing leading–edge vortex is placed closer to the wing surface suppressing also the large dead flow region at the wing root area.

Surveys of Turbulence Intensity

The turbulent flow structure is quantified by the rms values of the velocity fluctuations. They are typically nondimensionalized by the freestream velocity U_∞ to present the relative turbulence intensity in terms of percent of freestream. Here, only the axial rms component is considered, Figs. 13 to 16.

At $\alpha = 20$ deg and $x_W/l_W = 0.2$, the rms patterns of the wing–body configuration show two regions of high velocity fluctuations, Fig. 13a. At $Y = -1.01$ the peak rms value of 10% indicates the center of the wing tip vortex. Its viscous core is defined by the steep gradients in the lateral and vertical velocity (Fig. 10a) resulting

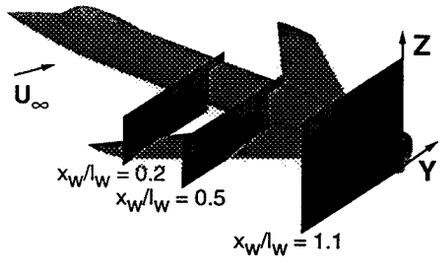

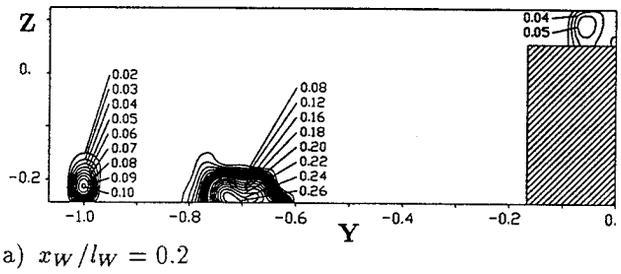

a) $x_W/l_W = 0.2$

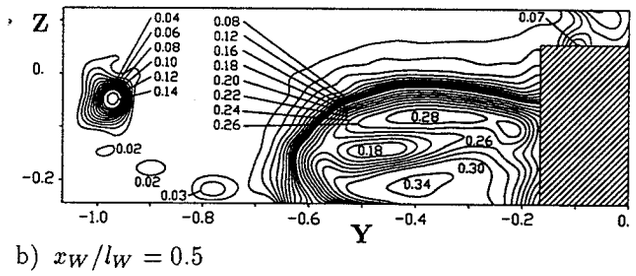

b) $x_W/l_W = 0.5$

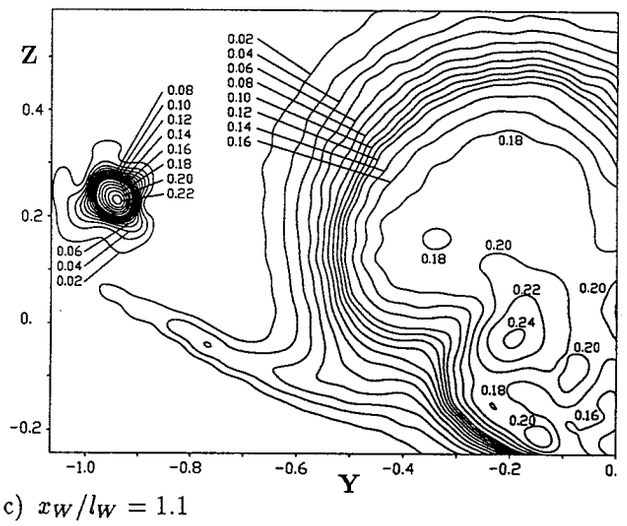

c) $x_W/l_W = 1.1$

FIGURE 13 – Contours of axial rms velocity u_{rms}/U_∞ for the wing–body configuration at measurement planes $x_W/l_W = 0.2, 0.5, 1.1$, and $\alpha = 20$ deg

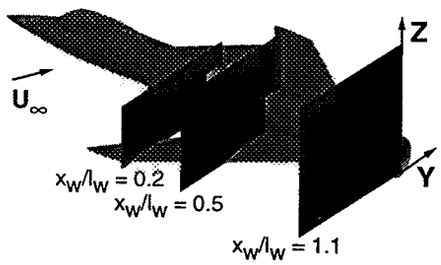

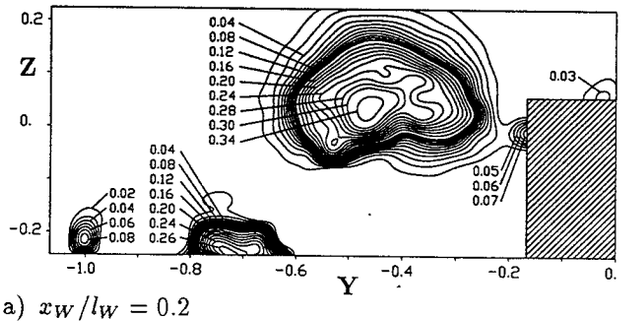

a) $x_W/l_W = 0.2$

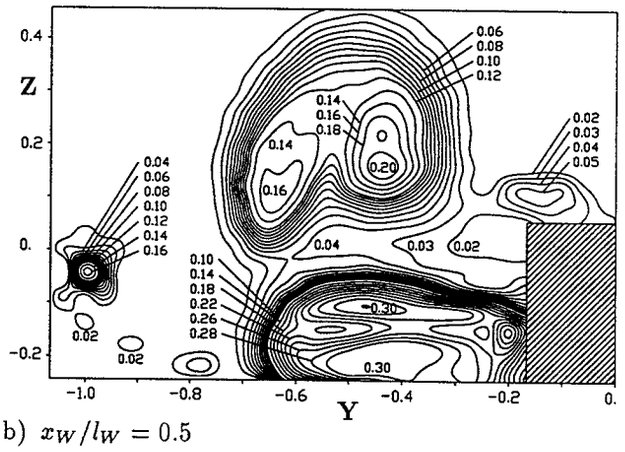

b) $x_W/l_W = 0.5$

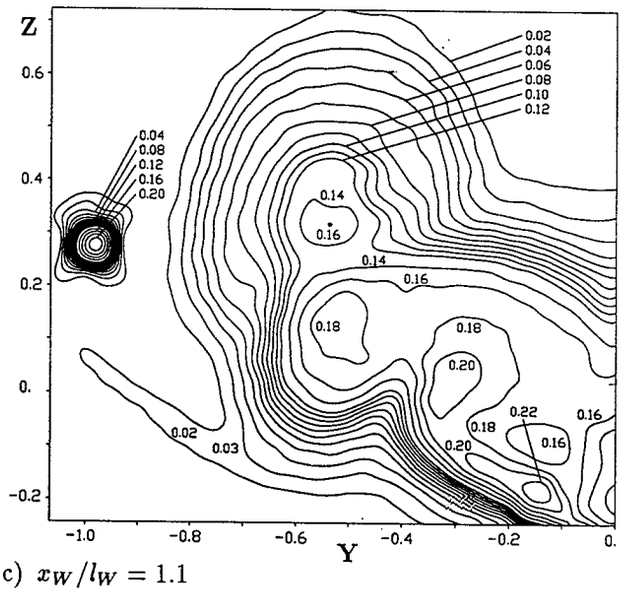

c) $x_W/l_W = 1.1$

FIGURE 14 – Contours of axial rms velocity u_{rms}/U_∞ for the wing–body–canard configuration at measurement planes $x_W/l_W = 0.2, 0.5, 1.1$, and $\alpha = 20$ deg

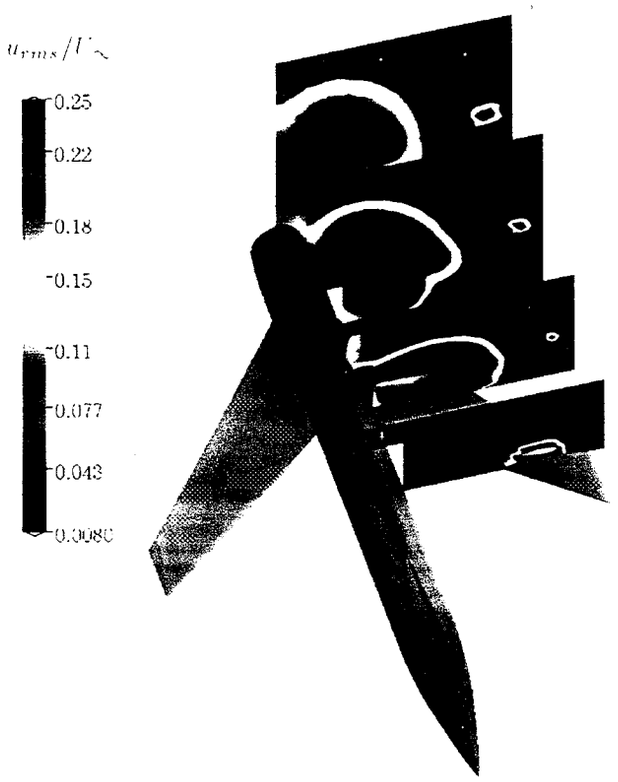

FIGURE 15 Axial turbulence intensity u_{rms}/U_∞ at cross flow planes $x_W/l_W = 0.2, 0.5, 0.8$ and 1.1 for the wing-body configuration at $\alpha = 30$ deg

in an increased turbulence level. The peak rms value of 26% at $Y = -0.72$ denotes the center of the wing leading-edge vortex. The substantially higher turbulence intensity is caused by the bursting process where the adverse pressure gradient leads to a stagnation of the axial flow near the vortex axis (Fig. 8a). A local turbulence maximum above the fuselage indicates a vortex pair shed at the canopy. The leading edge vortex is then considerably expanded at $x_W/l_W = 0.5$ covering the whole local span, Fig. 13b. Peak rms values reach levels of 34%. The pattern of the axial rms velocity associated with the burst leading edge vortex is significantly changed. The maximum turbulence intensity is now concentrated on a limited radial range relative to the vortex axis. It was found that such rms patterns are typical for burst leading edge vortices on slender delta wings.[20,24] The region of maximum turbulence intensity corresponds approximately to the points of inflection in the radial profiles of retarded axial velocity (Fig. 8b). Downstream of the wing trailing-edge at $x_W/l_W = 1.1$, the leading-edge vortex starts to dissipate, documented by the further enlargement of the turbulent region and the decrease in rms values, Fig. 13c. The merging process of the neighboured port and starboard vortex sheets supports the disintegration of the primary vortex. A warp in the lower vortex sheet at $Y = -0.3$ marks the region between the outboard leading edge vortex and the embedded inboard trail-

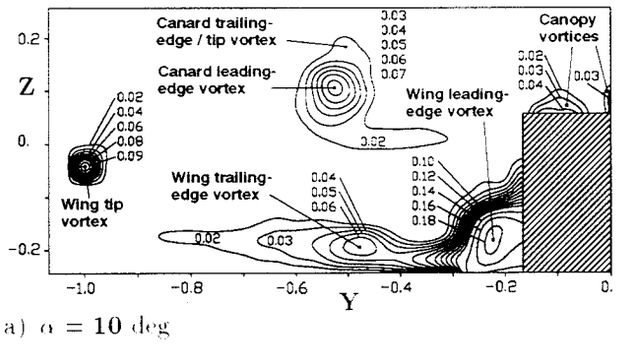

a) $\alpha = 10$ deg

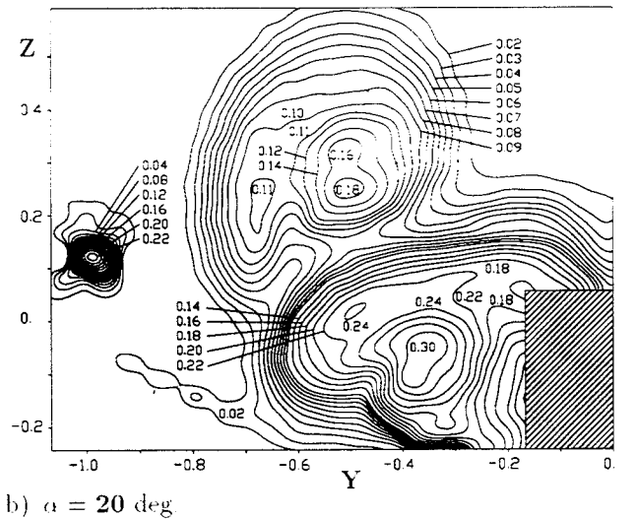

b) $\alpha = 20$ deg

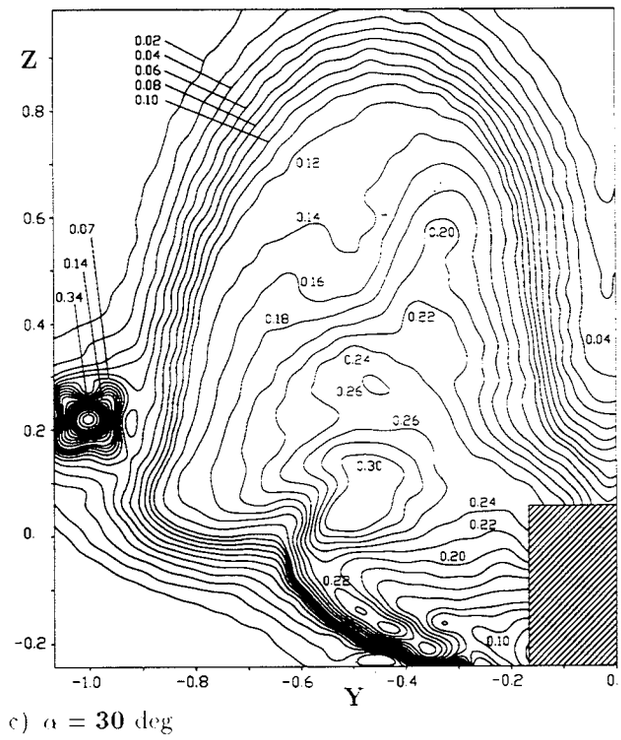

c) $\alpha = 30$ deg

FIGURE 16 - Contours of axial rms velocity u_{rms}/U_∞ for the wing-body-canard configuration at measurement plane $x_W/l_W = 0.8$, and $\alpha = 10$, 20, and 30 deg

ing edge vortex. For the canard–on configuration at $\alpha = 20$ deg and $x_W/l_W = 0.2$, the rms pattern for the wing tip and burst leading–edge vortex is very similar to that of the canard–off case, Fig 14a. The canard leading– and trailing–edge vortex pass relatively high above the wing leading–edge. Due to bursting, the canard vortex system is manifested by a large region of high velocity fluctuations even higher than that for the burst wing primary vortex. At $x_W/l_W = 0.5$, the canard vortex system is characterized by two clearly separated rms maxima, with the inboard rms maximum representing the leading–edge vortex, while the outboard rms maximum representing the trailing–edge vortex, Fig. 14b. Compared to the turbulence intensity of the upstream plane, the peak rms values are of lower magnitude. This, together with an increase in induced velocity (Figs. 9b, 11b) substantiates that over the wing, restoring of the canard vortex system takes place. The canard interference itself leads to a reduction of the very high velocity fluctuations occuring close to the wing surface. Downstream, the wing and canard vortex systems are strongly connected by their shear layers. Throughout the merging process, the turbulence intensity related to the wing and canard leading–edge vortex decreases, Fig 14c. This develops more extensively for the wing leading–edge vortex than for the canard one. However, the wing tip vortex is kept relatively strong and stable indicated by the less expanded circular region of the rms pattern and an increase in the peak rms values.

The annular structure of maximum turbulence intensity which is characteristic for the burst wing leading–edge vortex is also documented for the wing–body configuration at $\alpha = 30$ deg, Fig 15. There, the described rms pattern is already present at $x_W/l_W = 0.2$ due to the burst position which is located close to the wing tip. Further on, the distributions of axial velocity fluctuations are shown for the wing–body–canard configuration at $x_W/l_W = 0.8$, and $\alpha = 10$, 20 and 30 deg, Fig. 16. For better identification, the different vortices are marked in Fig. 16a. With increasing α there is a tremendous enlargement of high turbulence intensity regions associated with the canard and wing vortex systems, Fig. 16b. It is seen that this process is mainly dominated by the burst wing and canard leading–edge vortices. Thus, at high α the merging of wing and canard vortices result in an area of high flow fluctuations with a diameter of three times the fuselage height, Fig. 16c. Because of this, single– or twin–finned configurations would be prone to buffeting.

Spectral Content at High Angle of Attack

Spectral densities of the axial velocity fluctuations are evaluated at stations affected by the burst wing primary vortex, especially, within the limited radial range of maximum turbulence intensity. There, the spectra exhibit pronounced narrow–band peaks, Fig. 17.

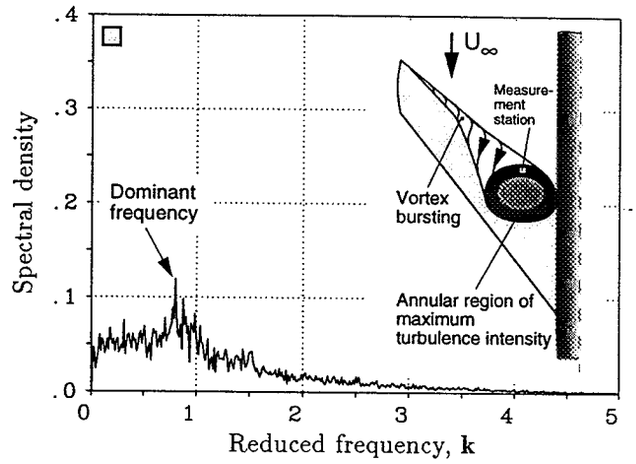

a) $\alpha = 20$ deg; $u_{rms}/U_\infty = 17.5\%$

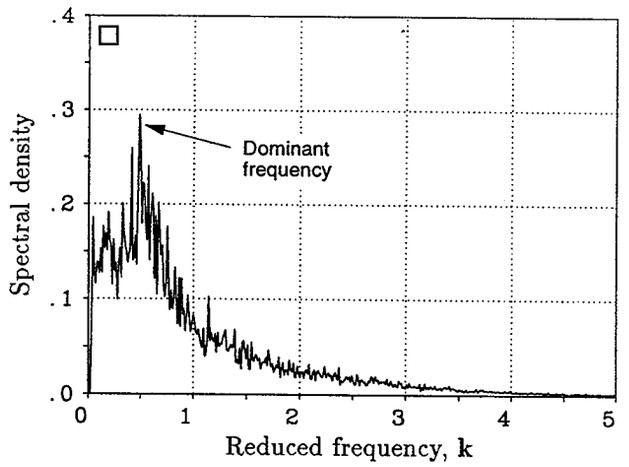

b) $\alpha = 30$ deg; $u_{rms}/U_\infty = 24.3\%$

FIGURE 17 – Spectra of the axial velocity fluctuations measured at the burst wing leading–edge vortex of the wing–body configuration at $\alpha = 20$ and 30 deg

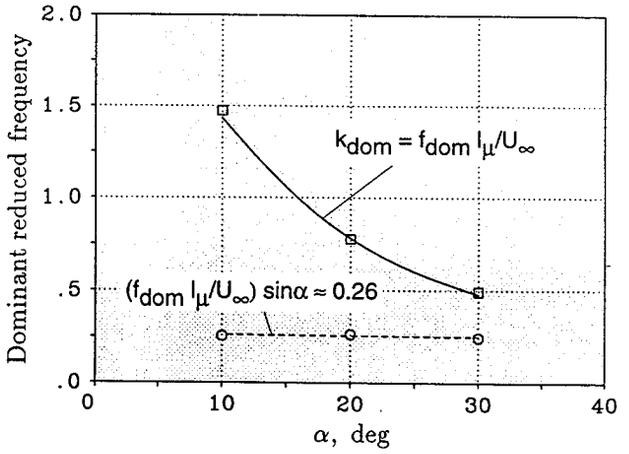

FIGURE 18 – Reduced frequency of the dominant spectral peaks as a function of angle of attack measured at the burst wing leading–edge vortex of the wing–body configuration

It shows that kinetic turbulent energy is channeled into a narrow band driven by quasi–periodic oscillations. This process is significant for the flow of burst leading–edge vortices, in particular, for the shear layer region around the expanded vortex core.[23] It was found that the pericodicity is linked to a helical mode instability with an azimuthal wave number of 1.[20,24] Under these conditions breakdown is the leading mechanism for quasi–peridodic loading on wing or fin(s).

Dominant Frequency

The dominant reduced frequencies according to the narrow–band spectral peaks decrease with increasing angle of attack. This is due to the growth of the burst vortex core through which wave lengths of the quasi–pericodic fluctuations increase while the related frequencies decrease. In order to scale for angle of attack, a reduced frequency parameter introducing the sinus of α is used. It is shown that for various α, the reduced frequency parameter $k \sin \alpha$ gives an approximate constant value of 0.26.

Conclusions

Extensive experimental investigations have been conducted on the low–speed flow environment of forward swept wing configurations. Models employed include a wing–body and a wing–body–canard configuration with wing sweeps of –40 deg. Advanced hot–wire anemometry is used to measure the time–dependent flowfield velocities in the cross flow planes located at three different stations over the wing and at one station in the wake. The surveys were taken at angles of attack of 10, 20 and 30 deg at a test Reynolds number of 0.46×10^6. The main results of these investigations are as follows:

1) On the wing–body and wing–body–canard configuration, complex vortex systems are present. For the canard–off case, the wing tip vortex and the wing leading–edge (primary) vortex with an opposite sense of rotation dominates the flowfield. At higher angles of attack, the wing primary vortex is accompanied by a weak secondary vortex. Moreover, the trailing–edge vortex sheet emanating from the inner wing part, rolls up to form a trailing–edge vortex. In the wake, the wing leading– and trailing–edge vortices merge, while the trailing–edge vortex is moved inboard and upwards.

2) Bursting of the wing leading–edge vortex occurs already at moderate angles of attack in the outer wing region.

3) At the canard–on configuration, the canard vortex system passes relatively high above the wing leading–edge. It consists of the canard's leading–edge vortex combined with a trailing–edge vortex and the canard's tip vortex. Through wing influence, this vortex system is moved upwards and outboard. Over the wing, the canard vortex system becomes reinforced, thus keeping its structure up to stations donwstream of the wing trailing–edge. At high α, an intensive merging takes place between the burst wing and canard vortices.

4) The rms distributions indicate the increase in turbulence intensity towards the center of the wing tip vortex as well as an overall maximum of turbulence intensity for the burst wing and canard leading–edge vortices. Peak values reach levels of 34% of U_∞. Downstream of bursting the maximum turbulence intensity is concentrated within a characteristic annular region.

5) At stations near the trailing–edge of the wing, the burst canard and wing leading–edge vortices are strongly expanded. This is associated with a large region of high turbulence intensity surrounding the midsection. Consequently, single– or twin–finned configurations may encounter severe buffet loads.

6) Distinct narrow–band spectral peaks are found in the wake of the burst wing leading–edge vortex. They indicate quasi–periodic oscillations which are proven to be typical for this flow type. For the dominant spectral peaks, a reduced frequency parameter scales approximately with the sinus of α.

References

1. Herbst, W. B., "Future Fighter Technologies," *Journal of Aircraft*, Vol. 17, No. 8, 1980, pp. 561–566.
2. Orlik–Rückemann, K. J., "Aerodynamic Aspects of Aircraft Dynamics at High Angles of Attack," *Journal of Aircraft*, Vol. 20, No. 9, 1983, pp. 737–752.
3. Barlow, R. C. and Keith Richey G., "Trends in Modern High Performance Aircraft," *Proc. Inter. Conf. Forward Swept Wing Aircraft*, Bristol, U.K., 24-26 March, 1982.
4. Zhang, B. and Laschka, B., "On Forward Swept–Wing's Aerodynamic Characteristics," *Journal of Northwestern Polytechnical University*, Vol. 7, No. 3, 1989, pp. 321–328.
5. Burns, B. R. A., "Vor– und Nachteile negativ gepfeilter Tragflügel," *Interavia*, No. 1, 1985, pp. 39–41.
6. du Boucheron, O. and Brocard, Y., "Comparison of Aerodynamic Characteristics of Aircraft Models with Forward and Aft Swept Wings at Mach Number 0.5," *Proc. Inter. Conf. Forward Swept Wing Aircraft*, Bristol, U.K., 24-26 March, 1982.

7. Zhang, B. and Laschka, B., "On Aerodynamic Characteristics of Canard in Canard–Forward–Swept Wing Configuration ," *Journal of Northwestern Polytechnical University*, Vol. 8, No. 3, 1990, pp. 327–334.
8. Nangia, R. K., "Aspects of Forward Swept Wing Research at the University of Bristol," *Proc. Inter. Conf. Forward Swept Wing Aircraft*, Bristol, U.K., 24-26 March, 1982.
9. Löbert, G., "Spanwise Lift Distribution of Forward– and Aft–Swept Wings in Comparison to the Optimum Distribution Form," *Journal of Aircraft*, Vol. 18, No. 6, 1981, pp. 496–498.
10. Schweiger, J., Schneider, G., Sensburg, O., and Löbert, G., "Design of a Forward Swept Wing Fighter Aircarft," *Proc. Inter. Conf. Forward Swept Wing Aircraft*, Bristol, U.K., 24-26 March, 1982.
11. Nangia, R. K. and Shaw, D. E., "Theoretical Investigations into Forward Swept Wings," *Proc. Inter. Conf. Forward Swept Wing Aircraft*, Bristol, U.K., 24-26 March, 1982.
12. Stanniland, D. R., "Aspects of the Aerodynamic Design of a Thin, Supercritical, Forward Swept Wing for a Combat Aircraft," *Proc. Inter. Conf. Forward Swept Wing Aircraft*, Bristol, U.K., 24-26 March, 1982.
13. Weeks, T. M. and Leet, L. H., "The X–29A Forward Swept Wing Advanced Technology Demonstrator Program," *Proc. Inter. Conf. Forward Swept Wing Aircraft*, Bristol, U.K., 24-26 March, 1982.
14. Griffin, K. E., "Measurement of Wake Interactions of a Canard and a Forward Swept Wing," USAFA–TN–82-4, U.S. Air Force Academy, Colorado Springs, CO, July 1982.
15. Griffin, K. E., Haerter, E. C., and Smith, B. R., "Wake Characteristics and Interactions of the Canard/Wing Lifting Surface Configuration of the X–29 Forward Swept Wing Flight Demonstrator," USAFA–TN–83-7, U.S. Air Force Academy, Colorado Springs, CO, Aug. 1983.
16. Griffin, K. E. and Jonas, F. M., "Wake Characteristics and Interactions of the Canard/Wing Lifting Surface Configuration of the X–29 Forward Swept Wing Flight Demonstrator," AIAA Paper 83–1835, AIAA Applied Aerodynamics Conf., July 13-15, 1983.
17. Breitsamter, C., "Vortex–Dominated Flowfields at Forward Swept Wing Configurations," *Jahrbuch des Deutschen Luft– und Raumfahrtkongresses/ DGLR–Jahrestagung*, Vol. I, München, 14.-17. Okt., 1997, pp. 517–526.
18. Bendat, J. S., and Piersol, A. G., "Random Data: Analysis and Measurement Procedures," J. Wiley & Sons, Inc. New York, 1971.
19. Breitsamter, C. and Laschka, B., "Velocity Measurements with Hot–Wires in a Vortex–Dominated Flowfield. AGARD–CP–535, *Wall Interference, Support Interference and Flow Field Measurements*, Brussels, Belgium, Oct. 4-7, 1993, pp. 11-1–11-13.
20. Breitsamter, C. "Turbulente Strömungsstrukturen an Flugzeugkonfigurationen mit Vorderkantenwirbeln," Dissertation, DM 18432, Technische Universität München, 1997.
21. Rohne, W., "Experimentelle Untersuchung des Strömungsfeldes und der aerodynamischen Größen an einer vorwärtsgepfeilten Flugzeugkonfiguration," Diplomarbeit FLM–95/32, Lehrstuhl für Fluidmechanik, Technische Universität München, 1995.
22. Tobak, M., and Peak, D. J., "Topology of Threedimensional Separated Flows," *Ann. Rev. Fluid. Mech.*, 14, 1982, pp. 61–85.
23. Breitsamter, C., and Laschka, B., "Turbulent Flow Structure Associated with Vortex–Induced Fin Buffeting," *Journal of Aircraft*, Vol. 31, No. 4, 1994, pp. 773 – 781.
24. Breitsamter, C., "Experimental Studies of the Turbulent Flow Structure of Leading–Edge Vortices," *Notes on Numerical Fluid Mechanics*, New Results in Numerical and Experimental Fluid Mechanics, Vol. 60, 1997, pp. 79–86.